

# Onsager Condensation in Chiral Active Matter: Universality of Topological Gas Dynamics

Magnus F Ivarsen\*

Department of Physics and Engineering Physics, University of Saskatchewan, Saskatoon, Canada

We identify a thermodynamic phase transition in chiral active matter. Low-frequency disorder triggers global synchronisation and energy dissipation, while high disorder activates a *topological heat pump*, generating an inverse energy cascade. This drives the system towards an Onsager dipole, which can be arrested into a metastable vortex glass if dispersion is insufficient to overcome the defect lattice. We propose topological gas dynamics as a universality class governed by the interplay of active disorder and topological sorting, unifying active swarms and classical inviscid fluids.

## INTRODUCTION

Active turbulence, the chaotic spatiotemporal dynamics observed in bacterial swarms [1, 2], cytoskeletal extracts [3], and synthetic colloidal flocks [4, 5], presents a challenge to statistical physics. Unlike classical inertial turbulence, which is driven by high Reynolds numbers ( $R_e$ ), active turbulence arises in the overdamped limit ( $R_e \approx 0$ ), driven by the continuous injection of energy at the microscale [6, 7].

Despite the viscous dominance in such systems, observations frequently reveal large-scale coherent structures reminiscent of inertial fluid flows [8]. This has ignited a debate regarding the universality class of active matter [3]. Current theories, largely built on the hydrodynamics of active nematics, predict steep energy spectra (typically  $E(k) \sim k^{-4}$  or  $k^{-3}$ ) dominated by the proliferation of half-integer defects [9, 10]. While such models successfully describe transient pattern formation, they generally fail to predict the robust inverse energy cascades ( $k^{-5/3}$ ) observed in chiral active fluids [11] and 2D quantum turbulence [12].

The discrepancy implies a missing link in the theoretical framework concerning active matter dynamics. While the role of odd viscosity (or Hall viscosity) in chiral active matter has been identified as a mechanism for breaking parity and enabling unidirectional flow [13, 14], the thermodynamic end-state of such systems remains largely unexplored. Specifically, does the breaking of detailed balance (time reversal symmetry breaking [15]) by intrinsic rotation merely sustain a chaotic steady state, or does it drive the system toward a specific macroscopic attractor?

In this Letter, we propose that the answer to the conundrum lies in *topological gas dynamics*. By simulating chiral active matter as an ensemble of  $N$  locally phase-coupled oscillators experiencing a Kuramoto-like phase-interaction [16, 17], we demonstrate that chiral active matter can act as a dual-phase system: a microscopic active bath dominated by enstrophy injection ( $k^{-3}$ ), and a macroscopic renormalised fluid element governed by the conservative advection of topological defects. By filtering out the microscopic singularities, we reveal that the simulated system undergoes a “hidden” inverse en-

ergy cascade with a Kolmogorov-scaling ( $k^{-5/3}$ ), indistinguishable from Euler (frictionless, inviscid) turbulence. This cascade functions as a thermodynamic pump, driving the system toward an *Onsager dipole*, a negative-temperature condensate of vorticity [18], thereby unifying the phenomenology of biological swarms with the rigorous statistical mechanics of point vortices.

## METHODOLOGY

### The Model

We define the system as a chiral active fluid composed of  $N = 50,000$  particles, or discrete agents, in a bounded periodic domain  $\mathcal{D} \in \mathbb{R}^2$ . The state of the  $i$ -th agent is defined by its position  $\mathbf{r}_i(t)$  and its internal phase  $\phi_i(t) \in [0, 2\pi]$ .

The agents do not interact via pairwise collisions (as in granular matter) but through a local mean field. Following Ref. [16], we define the complex order parameter field  $Z(\mathbf{r}, t)$  as the convolution of the microscopic agent distribution with a finite-range interaction kernel  $G$ :

$$Z(\mathbf{r}, t) = R(\mathbf{r}, t) e^{i\Psi(\mathbf{r}, t)} = \int_{\mathcal{D}} G(|\mathbf{r} - \mathbf{r}'|) \left[ \sum_{j=1}^N \delta(\mathbf{r}' - \mathbf{r}_j(t)) e^{i\phi_j(t)} \right] d\mathbf{r}', \quad (1)$$

where  $G(|\mathbf{r} - \mathbf{r}'|)$  is the Green’s function of the interaction (modeled as a Gaussian with kernel size  $\sigma$ ),  $R(\mathbf{r}, t)$  is the local coherence (or order parameter, where  $R \approx 1$  implies high local synchronisation and  $R \approx 0$  implies a phase singularity, or defect core).  $\Psi(\mathbf{r}, t)$  is the local mean phase. The convolution kernel  $G$  is interpreted in the context of chemical gradients or electric fields, which govern the dense active matter interactions (e.g., bacterial swarms or even electron gases). By modifying  $G$ , we can potentially simulate anisotropic media (like magnetized plasmas) without changing the agent logic.

Following Ref. [16], the internal phase  $\phi_i$  evolves according to an overdamped, localized, driven Kuramoto-

Sakaguchi-like interaction [19, 20]:

$$\dot{\phi}_i = \underbrace{\omega_i}_{\text{Driver}} + \underbrace{a_0 R(\mathbf{r}_i) \sin(\Psi(\mathbf{r}_i) - \phi_i)}_{\text{synchronisation force}} + \underbrace{\sqrt{2D_\phi} \eta_i(t)}_{\text{Stochastic noise}}, \quad (2)$$

where  $\omega_i$  are natural frequencies drawn from a power-law distribution  $P(\omega) \sim \omega^{-\gamma}$ ,  $a_0$  is the coupling Strength, and  $\eta_i$  is a Gaussian white noise term.  $R_i$ , the local order parameter, ensures that synchronisation is triggered by initially random local alignments in phase.  $\omega_i$  (and the stochastic term  $\eta_i$ ) prevent a “ferromagnetic collapse”, in which the system simply synchronises globally ( $\phi_i = \text{const}$ ), stopping all motion (or causing a uniform ballistic drift). By forcing the particles to oscillate with an inherent frequency (or attempt to), the  $\omega_i$  terms act as frustration, constantly injecting vorticity at the micro-scale, which, as we shall demonstrate, feeds an inverse energy cascade.

The definitive equation of this model, distinguishing it from standard fluids, is the non-inertial slave principle, or agent-based equation of motion [21, 22], where the velocity vector is explicitly determined by the instantaneous phase:

$$\dot{\mathbf{r}}_i = \mathbf{v} = v_0(\cos \phi_i, \sin \phi_i), \quad (3)$$

where  $\mathbf{r}_i = (x_i, y_i)$ . The particles are therefore without conventional inertia:  $\sum \mathbf{F} \neq m\mathbf{a}$ ; the system is fully overdamped, in a low Reynolds number limit [23]. In addition, we observe that if the phase field forms a vortex (phase singularity or topological defect), the velocity field must also form a vortex, introducing singularities in the vorticity field  $\nabla \times \mathbf{v}$ . To define a valid continuum fluid, we introduce the renormalised fluid element (RFE).

A natural definition of the RFE is given by the mean-field kernel size  $\sigma$  in our model (Eq. 2),

$$\tau = \frac{\sigma}{v_0} = \frac{3 \text{ grid units}}{0.5 \text{ grid units/s}} = 6 \text{ s.}$$

We define the RFE as the center of mass of a particle’s trajectory during  $\tau$ , effectively course-graining the singularities:

$$R_i = \text{angle} \left( \frac{1}{\tau} \sum_{t'=t-\tau}^t \hat{r}_i(t') \right) \cdot \frac{L}{\pi}, \quad (4)$$

with  $L$  being the domain half-width, and,

$$\hat{r}_i(t) = \exp \left( i \cdot \frac{r_i(t)}{L} \cdot \pi \right), \quad (5)$$

being the complex phasor locations mapped to a unit circle (necessitated by the periodic boundary conditions). The transformation Eq. (4) constitutes the regularization of the topological defects in  $\phi_i$ , which become physical flow vortices in  $\mathbf{r}_i$ .

The kernel width  $\sigma$  defines the correlation length of the local mean field, establishing a natural scale separation. We define the cut-off wavenumber  $k_c \equiv 2\pi/\sigma$ , which, as we shall demonstrate, marks the transition between the microscopic active bath ( $k > k_c$ ) and the macroscopic hydrodynamic limit ( $k < k_c$ ). The RFE operator effectively acts as a low-pass filter with cut-off  $k_c$ , isolating the collective, fluid modes.

### Theoretical foundation

To bridge the discrete dynamics and the continuum fluid, we define the macroscopic velocity field  $\mathbf{u}(\mathbf{r}, t)$  as the local average of the particle velocities. Decomposing the particle phase into the local mean phase  $\Psi$  and a fluctuation  $\delta\phi_i$  (that is,  $\phi_i = \Psi + \delta\phi_i$ ), and assuming symmetric fluctuations (that is,  $\langle \sin \delta\phi \rangle \approx 0$ ), the coarse-grained velocity becomes

$$\mathbf{u} = \langle \mathbf{v}_i \rangle \approx v_0 \langle \cos \delta\phi \rangle (\cos \Psi, \sin \Psi), \quad (6)$$

where we identify the local order parameter  $R$ ,

$$R_n = \langle \cos(n\delta\phi) \rangle = \text{Re} [\langle e^{in\delta\phi} \rangle], \quad (7)$$

for a peaked (narrow) Gaussian distribution in  $\delta\phi$ .  $R$  measures the degree of local synchronisation, and so the macroscopic speed is scaled by local synchronisation:

$$|\mathbf{u}| = v_0 R. \quad (8)$$

Thus, while individual particles move at constant speed  $v_0$ , the renormalised fluid element speed is variable and proportional to the local synchronization. To express  $\mathbf{u}$  in terms of the field potential  $\Psi$ , we identify the flow direction  $\hat{\mathbf{n}} = (\cos \Psi, \sin \Psi)$  with the normalized phase gradient:

$$\mathbf{u} = v_0 R \frac{\nabla \Psi}{|\nabla \Psi|}. \quad (9)$$

Eq. (9) is globally valid: at defect cores where the phase  $\Psi$  is undefined, the order parameter vanishes ( $R \rightarrow 0$ ), ensuring the velocity field remains continuous and bounded ( $\mathbf{u} \rightarrow 0$ ). Recognizing that  $\nabla \Psi$  scales as  $1/r$  near defects, we note that the vector  $\mathbf{u}$  is parallel to  $\nabla \Psi$ . Far from defect cores, where the phase gradient magnitude varies slowly ( $|\nabla \Psi| \approx \text{const}$ ), the flow simplifies to an effective potential flow:

$$\mathbf{u} \approx R \nabla \Psi. \quad (10)$$

This approximation allows us to utilize the machinery of inviscid fluid mechanics in the bulk of the domain, while the factor  $R$  naturally regularizes the dynamics at the topological singularities (see Appendix B for additional details).

The continuity equation for  $\mathbf{u}$  then reads,

$$\frac{\partial \rho}{\partial t} + \nabla \cdot (\rho \mathbf{u}) = 0. \quad (11)$$

Substituting Eq. (10) into Eq. (11), we observe that the macroscopic density evolution is governed by mean phase curvature:

$$\frac{\partial \rho}{\partial t} \approx -v_0 R \nabla \cdot (\rho \nabla \Psi). \quad (12)$$

This formulation identifies the system as analogous to the shallow water equations [24, 25], where the active density  $\rho$  acts as the fluid height. The phase curvature  $\nabla^2 \Psi$  drives the compression of the fluid elements, explicitly linking topological defects to density fluctuations. Consequently, the inviscid Euler behaviour that we observe in the RFE field in the next section represents the *low-Mach-number limit of a compressible system*, where the rotational, non-compressive wave modes decouple from and energetically dominate the irrotational, compressive wave (acoustic) modes at large scales.

The hydrodynamic closure is completed by the momentum equation. The non-linearity of the phase evolution generates velocity fluctuations, which manifest as an active Reynolds stress  $\sigma_{ij} \sim \langle \delta v_i \delta v_j \rangle$ . As we derive in Appendix B, the renormalization of this stress yields the effective inertial advection term  $\lambda(R)(\mathbf{u} \cdot \nabla)\mathbf{u}$ . Here, the coefficient  $\lambda(R) \approx R^2$  functions as an *emergent inertial mass* determined by local synchronization. This renders the macroscopic momentum transport isomorphic to that of an Euler fluid. Consequently, the motion of topological defects decouples from the overdamped microscopic kinetics, governed instead by the inertial advection of the renormalised superfluid.

Finally, we identify the topological conservation law that governs the renormalised fluid. As the phase  $\Psi(\mathbf{r})$  is derived from a complex scalar field, its circulation along any closed loop  $\partial\Sigma$  enclosing a defect core is quantized [16, 26]:

$$\oint_{\partial\Sigma} \nabla \Psi \cdot d\mathbf{l} = 2\pi m, \quad (m \in \mathbb{Z}). \quad (13)$$

Assuming isotropy in the renormalised fluid, this geometric constraint implies  $|\nabla \Psi| = m/r$ . Substituting this into our macroscopic velocity definition (Eq. 9), and assuming the order parameter  $R$  is locally uniform, the fluid velocity induced by a defect scales as:

$$|\mathbf{u}| \approx v_0 R \frac{m}{r}. \quad (14)$$

This confirms that the topological defects of the mean phase act as point vortices with an effective physical circulation  $\Gamma_{eff} \approx 2\pi m v_0 R$ . Consequently, the interaction energy of the ensemble is given by the Kirchhoff-Onsager Hamiltonian [27, 28]:

$$H = - \sum_{i \neq j} \Gamma_i \Gamma_j \ln |\mathbf{r}_i - \mathbf{r}_j|. \quad (15)$$

Crucially, this derivation highlights that the topological charge driving the Hamiltonian dynamics is scaled by

the order parameter  $R$ . If renormalization is suppressed ( $R \rightarrow 0$ ), the effective circulation vanishes ( $\Gamma_{eff} \rightarrow 0$ ), causing the Hamiltonian interaction to collapse and the system to arrest.

### The Onsager attractor

In a bounded domain  $\mathcal{D}$ , the phase space volume  $\Omega(E)$  (the number of ways to arrange vortices with total energy  $E$ ) eventually *decreases* as the energy increases. In the low-energy limit, vortices are paired (dipoles), screening each other. In the high-energy limit, like-signed vortices must cluster together to maximize the distance between positive and negative clumps. The result is that  $\frac{dS}{dE} < 0 \implies T < 0$  [18]. As we shall demonstrate, our simulation therefore resembles a *heat pump* (injecting enstrophy via  $\omega_i$ ), driving the system up the energy ladder until it enters the negative temperature regime, manifesting as the macroscopic Onsager dipole.

### Spectral scaling

This framework predicts a spectral dichotomy based on the scale of observation. At the microscopic scale, the raw particle field is dominated by the singular geometry of the phase defects ( $\nabla \phi \sim 1/r$ ), forcing the system into the enstrophy-dominated regime with a steep spectral index  $E_{raw}(k) \sim k^{-3}$  [29–32]. Conversely, the macroscopic dynamics are governed by the Kirchhoff-Onsager Hamiltonian (Eq. 15), which describes an effective inviscid (frictionless) fluid. The RFE field, which filters out the microscopic singularities, will therefore recover the classical inverse energy cascade signature, exhibiting the Kolmogorov scaling  $E_{RFE}(k) \sim k^{-5/3}$  [12, 33]. The renormalization unifies the dissipative phenomenology of active matter with the conservative statistical mechanics of Euler fluids.

We quantify the non-linear transfer of energy across scales using the standard spectral flux  $\Pi(k)$ , defined via the advective transport term  $(\mathbf{v} \cdot \nabla)\mathbf{v}$  characteristic of fluid turbulence,

$$\Pi(k) = - \int_0^k T(k') dk', \quad (16)$$

where the energy transfer function  $T(k)$  is defined as [34],

$$T(k) = \sum_{|\mathbf{q}|=k} \text{Re} \left[ \hat{\mathbf{v}}_{\mathbf{q}}^* \cdot \mathcal{F} \{ -(\mathbf{v} \cdot \nabla)\mathbf{v} \}_{\mathbf{q}} \right], \quad (17)$$

which sums contributions of all discrete wave vectors  $\mathbf{q} = (q_x, q_y)$  that fall within the annular shell where the magnitude  $|\mathbf{q}| \approx k$ , to the real part of the Fourier transform of the advective transport term, where  $\hat{\mathbf{v}}_{\mathbf{q}}^*$  is the complex conjugate of the velocity field in Fourier space at wave vector  $\mathbf{q}$ . A negative plateau in  $\Pi(k)$  would conclusively demonstrate an inverse cascade.

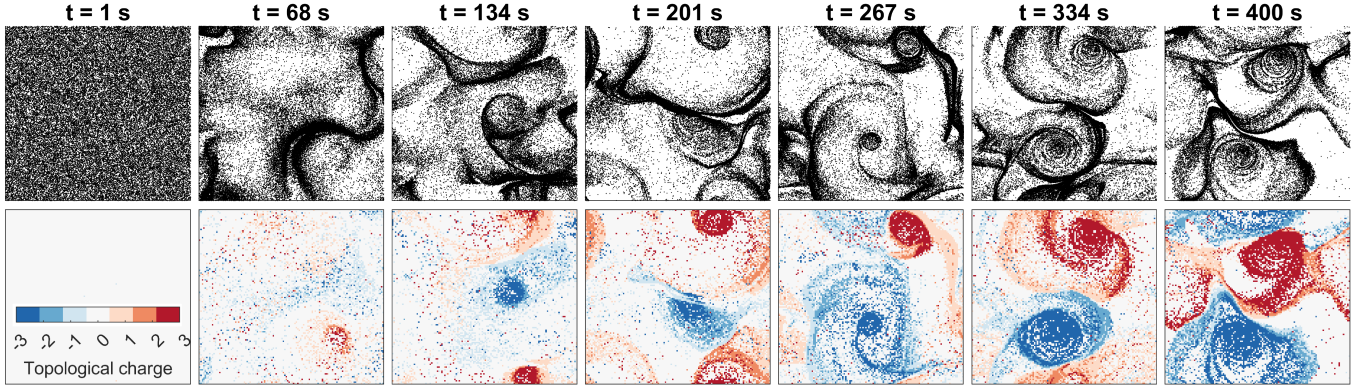


FIG. 1. **The emergence of the Onsager dipole in chiral active matter simulation**, shown by the simulation’s evolution through seven temporal snapshots, with top row representing the raw particle point-clouds while the bottom row plots topological charge (winding number, Eq. 13) with a colorscale.

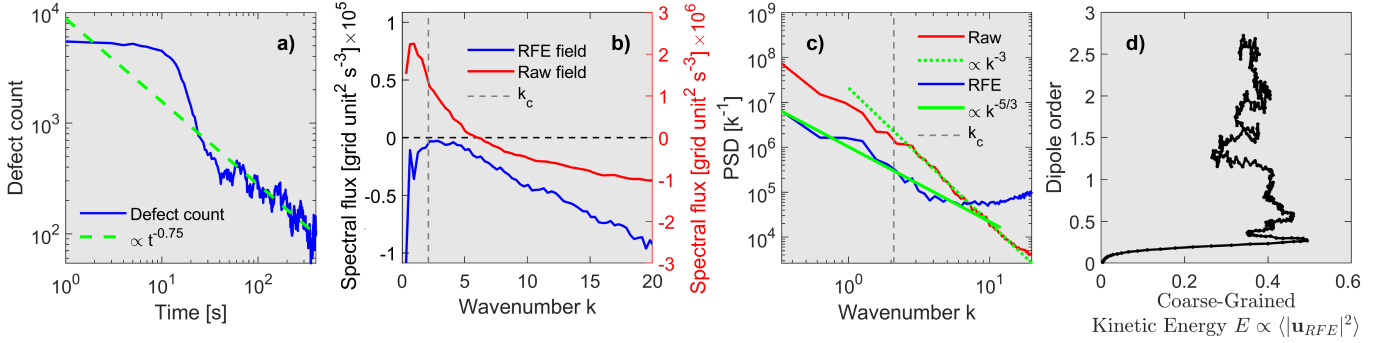


FIG. 2. **Energy characteristics of the simulation run in Figure 1.** **Panel a)** shows the defect (phase singularity) count, with a  $t^{-0.75}$  powerlaw scaling [35] with a dashed, green line. **Panel b)** shows the spectral flux (Eq. 16) for the RFE (blue, left  $y$ -axis) and raw (red, right  $y$ -axis) fields, taking the median of the entire simulation. **Panel c)** shows the energy spectrum  $E(k)$  for the RFE (blue) and raw (red) fields; a spectral scaling of  $k^{-5/3}$  and  $k^{-3}$  is indicated with dotted and solid green lines respectively. **Panel d)** shows the thermodynamic trajectory, plotting order versus coarse-grained kinetic energy for the simulation evolution. the cut-off wavenumber  $k_c$  is indicated with a dashed, grey line in panels b) and c), coinciding with spectral break-points, demonstrating the physical basis for the RFE operator (Eqs. 4–5).

## RESULTS

The temporal evolution of the system reveals a spontaneous transition from microscopic chaos to macroscopic order (Figure 1). Initially ( $t < 10s$ ), the system is dominated by small-scale phase defects that nucleate and annihilate rapidly. However, as the system evolves, surviving defects begin to cluster and merge, and by  $t = 200s$ , the flow is dominated by a sloshing, large-scale Onsager dipole.

To elucidate the mechanism driving this condensation, we analyzed the kinetic pathways of the topological defects (Figure 2b), the decay of the defect number density  $N_d(t)$ . Here, adherence to the theoretical  $t^{-0.75}$  scaling for vortex packing [35], significantly slower than the diffusive  $t^{-1}$  rate, confirms that vortex interaction is governed by long-range strain fields (vortex thinning [36, 37]) rather than random-walk annihilation [38, 39].

The directionality of the energy transfer is established

by the spectral energy flux  $\Pi(k)$  (Figure 2c), where the distinct negative plateau in the spectral flux ( $\Pi(k) < 0$ ) rigorously proves the inverse directionality of the energy cascade; energy injected at the microscale by  $\omega_i$  is transported upscale to the box size,  $\sim 2L$ , creating the Onsager dipole.

A central finding of this work is the resolution of the spectral dichotomy observed in active matter, namely the coexistence of steep, dissipative spectra with large-scale coherent structures [12, 40, 41]. Figure 2d) shows that raw particle velocity field exhibits a steep spectral slope  $E_{\text{raw}}(k) \propto k^{-3}$ , consistent with dissipative enstrophy [29]. This reflects the singular geometry of the topological defects: the raw agents are kinematically pinned to the sharp cusps of the phase field ( $\nabla\phi \sim 1/r$ ), and thus their spectrum measures the packing of vorticity filaments [42], exactly analogous to forced two-dimensional turbulence [32].

However, when we apply the RFE operator to the

ensemble, filtering out the microscopic singularities by averaging over the interaction scale  $\tau$ , a “hidden” Kolmogorov scaling is revealed: The RFE spectrum  $E_{RFE}(k)$  (the blue spectrum in Figure 2d) tracks the classical  $k^{-5/3}$  slope characteristic of 2D inviscid fluid turbulence, confirming our hypothesis that the chiral active matter (the oscillatory particles) acts as a dissipative kinetic layer that drives, through inverse cascade, a superfluid (the RFE field) governed by the conservative Kirchhoff-Onsager Hamiltonian.

Finally, we demonstrate that the formation of the dipole is a thermodynamic inevitability. Figure 2d) maps the system’s trajectory in the energy-order phase plane ( $E$  vs.  $P$ ). The system climbs monotonically away from the disordered origin (random gas), increasing both its macroscopic kinetic energy and its dipole order parameter  $P$ . In the context of the point-vortex Hamiltonian, this trajectory corresponds to an ascent up the entropy curve into the regime of negative absolute temperature [18]. The intrinsic disorder ( $\omega_i$ , or rather, the distribution  $\Delta\omega$ ) continuously injects enstrophy to maximize the entropy of the renormalised fluid, forcing the spectral condensation of vorticity as the only accessible maximum-entropy state within the bounded domain. This unifies the phenomenology of chiral active swarms with the rigorous statistical mechanics of classical inviscid fluids.

## DISCUSSION

Our results resolve a spectral paradox [4, 43–45] by demonstrating that chiral active matter may not be governed by a single physical regime, but by a scale-dependent duality. At the microscopic scale ( $k > k_c$ ), the system is dominated by phase singularities, with a steep spectral slope ( $E_{\text{raw}} \propto k^{-3}$ ) [29–32]; this is not a signature of dissipation, but of enstrophy injection, the active stretching and packing of vorticity filaments [36, 37]. This layer acts as a thermodynamic furnace that converts intrinsic chemical energy (represented by  $\omega_i$ ) into topological charge.

At macroscopic scales ( $k < k_c$ ), the system reveals a hidden renormalised fluid. By filtering out the singular defects via the RFE operator (Eqs. 4–5), we recover the Kolmogorov- $k^{-5/3}$  inverse cascade. This implies that the collective motion of the defects generates a “phantom inertia,” an effective advective term,  $(\mathbf{v} \cdot \nabla)\mathbf{v}$  (see Appendix B), arising from the effective, active stress tensor, which then drives the system according to the laws of *inviscid hydrodynamics*, despite the overdamped nature of the individual agents.

The thermodynamic trajectory (Figure 2d) takes the system to the inevitable Onsager dipole, confirming that the system continuously maximizes its macroscopic entropy by climbing the energy ladder into the regime of negative absolute temperature [18].

Crucially, the RFE framework suggests a general res-

olution for the non-universal spectra frequently reported in biological and active matter experiments [9]. We propose that the deviations from Kolmogorov scaling observed in bacterial swarms, active nematics, and cytoskeletal gels [1, 3, 7, 9, 10, 46] may be artifacts of analyzing the raw particle fields rather than the renormalised hydrodynamic modes. By applying the RFE operator (Eqs. 4–5), essentially a low-pass filter, it may be possible to unveil hidden inertial-like scaling laws in a broad class of overdamped systems.

## Topological gas dynamics

While the RFE analysis confirms the existence of an underlying hydrodynamic skeleton ( $k^{-5/3}$ ), the realization of the Onsager dipole depends strictly on the system’s ability to overcome topological energy barriers (see, e.g., Ref. [17]). As alluded to by Ref. [16], we find that the intrinsic frequency dispersion  $\Delta\omega$  acts as an enstrophy injection rate for the topological gas, determining whether the system freezes, jams, or flows.

Figure 3 illustrates the foregoing by presenting the evolution of a simulation that used a narrower, lower-frequency dispersion  $\Delta\omega$  (see Figure 4 in the Appendix A); the raw particle distribution subsequently drove an inverse cascade, but the renormalised fluid did not, and the active bath was unable to transfer energy to wavenumbers  $k < k_c$ , resulting in an *arrested topological defect glass state*. While the Onsager fluid exhibits continuous, power-law coarsening ( $N \propto t^{-0.75}$ ), the vortex glass state exhibits a rapid localized quench ( $N \propto t^{-2}$ ) followed by a kinetic arrest ( $N \rightarrow \text{const.}$ ), yielding a complete absence of topological sorting, but the clear presence of quantized loop currents of phase information [26]; we tentatively note that this may constitute a novel state of matter.

Conversely, the Onsager dipole state, which represents the hydrodynamic limit, is in a *marginal synchronisation regime*, meaning that the synchronising force is in fact negligible for the instantaneous angular velocity, but maintains a non-zero order parameter  $R$  (facilitating flow). This is empirically confirmed by observing that the dynamics in Figure 1 effectively *never stop*. If  $R \rightarrow 1$ , the hydrodynamic limit is never reached, and the ensemble experiences a ferromagnetic-like collapse.

In Table I we summarize the results of varying the shape and magnitude of  $\Delta\omega$  (see Appendix A & B). This yields the stability boundaries of the topological gas dynamics and the thermodynamic Onsager attractor.

## CONCLUSION

We have identified a thermodynamic phase transition in chiral active matter, where intermediate disorder activates what resembles a topological heat pump that drives an inverse energy cascade ( $\Pi(k) < 0$ ). This cascade inevitably saturates in a negative-temperature *Onsager*

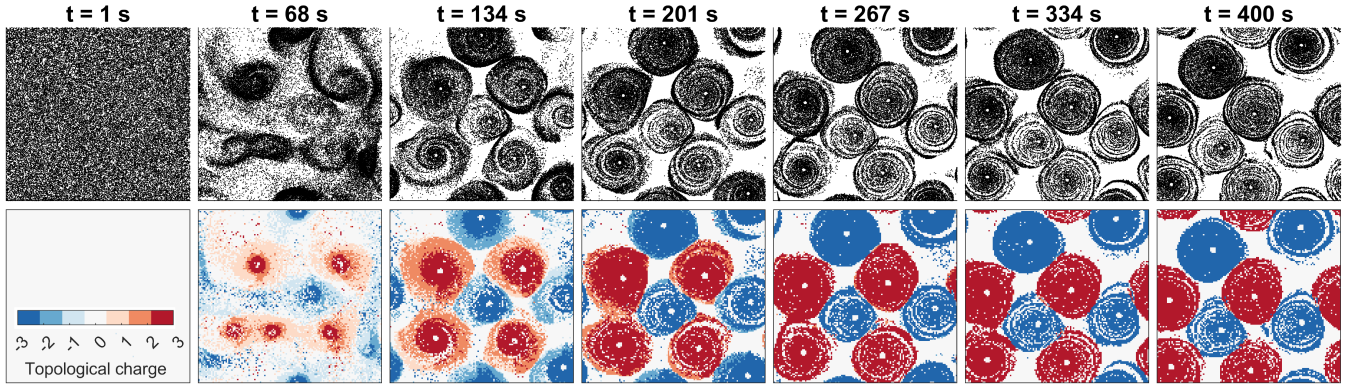


FIG. 3. **Active vortex glass** made of particles whose raw distribution features an inverse cascade ( $\Pi(k) < 0$ ), but whose RFE field features a forward-cascade ( $\Pi(k) > 0$ ). The defect count falls off drastically and flattens; defect merger is arrested and the ensemble settles in a frozen defect lattice. Top row shows the particle point-cloud while bottom row shows topological charge, while the columns correspond to seven temporal snapshots.

TABLE I. **Thermodynamic Phases of Chiral Active Matter.** The system state is determined by the intrinsic frequency dispersion  $\Delta\omega$ . High activity drives the inverse cascade towards the Onsager dipole, while low activity leads to kinetic jamming (glass).  $\Pi_{Raw}$  and  $\Pi_{RFE}$  refer to spectral flux for the raw particle distribution and the RFE field respectively. See Figure 6 in the End Matter for a rigorous characterization of the three phases.

| Phase                     | $\Delta\omega$               | Micro-Physics                      | Macro-State     | Signature                      |
|---------------------------|------------------------------|------------------------------------|-----------------|--------------------------------|
| I. Global synchronisation | $\Delta\omega \rightarrow 0$ | $\nabla\phi \rightarrow 0$ .       | Static clumps.  | $\Pi_{Raw} > 0, \Pi_{RFE} > 0$ |
| II. Active Vortex Glass   | Low / narrow                 | Frustration; no merger.            | Defect solid.   | $\Pi_{Raw} < 0, \Pi_{RFE} > 0$ |
| III. Onsager Condensate   | High / broad                 | Vortex merger via inverse cascade. | Onsager dipole. | $\Pi_{Raw} < 0, \Pi_{RFE} < 0$ |

*dipole*, a macroscopic ordered state protected by topological invariants. By distinguishing between the microscopic active bath and the macroscopic renormalised fluid, we provide a unified framework that explains the coexistence of seemingly dissipative spectra and inertial transport. These findings suggest that the large-scale organization of active matter may be governed by an inertia that emerges from topological constraints, offering a new paradigm for engineering robust transport in synthetic active fluids.

## END MATTER

This section provides the foundation for the phase diagram in Table I, through simulations that systematically vary the disorder distribution  $\Delta\omega$ , the source of the enstrophy injection, or frustration,  $\omega_i$ , in Eq. (2). First, however, we must outline a conjunction of two seemingly disparate turbulence theories.

### Appendix A: Three thermodynamic phases

Consider the theoretical turbulence frameworks of Ref. [17] (self-organisation) and Ref. [32] (forced hydrodynamics). The former describes an active, excitable medium of interacting fluctuations capable of self-organization, wherein a complex mean field amplitude

( $Z$ ) that arises from phase synchronisation acts as an effective force that traps individual stochastic oscillators into coherent clusters. The latter modeled a stable, self-similar dipole condensate that accumulates inverse-cascading energy at the system size, yielding a large-scale coherent vorticity  $\Omega$ .

Validating Ref. [17]’s concept of negative viscosity, we observe that our simulated active bath pumps energy from the injection scale to the system size, stabilizing the macroscopic state via multiplicative noise. This energy accumulation is remarkably analogous to the self-similar condensate characterized by Ref. [32], where the coherent dipole effectively slaves the background fluctuations to its global topology.

To conclude the theoretical conjunction, we show, in Figure 4, three distributions in  $\omega_i$ , corresponding to  $\Delta\omega$  in Table I. In our simulations, intrinsic frustration  $\omega_i$  near the box-size,  $1/2L$ , acts simultaneously as  $Z$  in Ref. [17] and  $\Omega$  in Ref. [32]. Thus, if the frustration dispersion  $\Delta\omega$  is too low and too narrow, the system generates active stress but lacks the transport coherence to move it, yielding an arrested glass vortex (Figure 3, Phase II in Table I). Reproducing a ferromagnetic-like collapse; a cold, isotropic, uniform “frustration” ( $\Delta\omega \rightarrow 0$ ) yields a collection of static clumps (Phase I in Table I). Conversely, if the dispersion in  $\omega_i$  is both sufficiently high and sufficiently broad (approaching the box-size), the system effectively facilitates the emergence

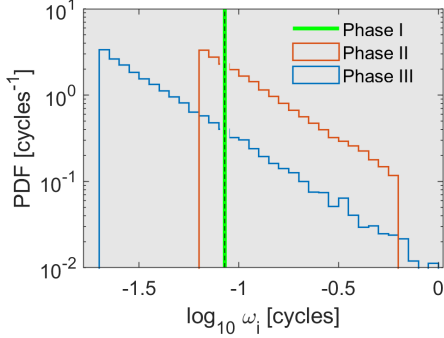


FIG. 4. The three distributions in  $\Delta\omega$  corresponding to the three thermodynamic phases in Table I, showing only the positive component ( $\omega_i$  is symmetric around 0). The upper limit on the  $x$ -axis corresponds to the maximum fluctuation  $1/2L$ .

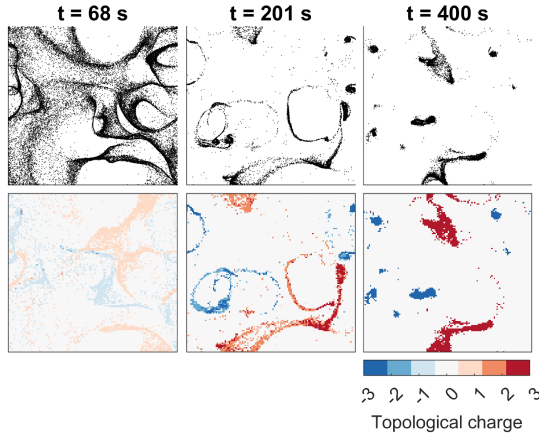


FIG. 5. **Summary of a Phase 1 simulation**, showing the evolution of static, phase-locked clumps. Upper row shows raw particle locations while bottom row shows topological charge with a colorscale.

of a space-filling Onsager dipole (Phase III in Table I).

In Figure 6 we rigorously demonstrate the foregoing by extracting the median results from 16 ensemble simulations of the three phases. Crucially, we observe that the spectral flux in Phase I (Figure 5) is positive for both the raw and RFE fields, while for Phase II (Figure 6f), the flux is negative for the raw field (crossing zero at intermediate wavenumbers) and positive for the RFE field, and for Phase III the flux is consistently negative, facilitating the inverse cascade that would otherwise be arrested in the case of Phase II.

Thus, by revealing that the hydrodynamic condensate characterized by Ref. [32] is the physical realization of the noise-induced phase transition predicted by Ref. [17], we have provided an independent proof of our central thesis, namely a unified theory of active chiral matter where microscopic phase synchronisation and macroscopic inverse cascades are understood as dual manifestations of the same thermodynamic attractor.

## Appendix B: Derivation of advective transport

In this section, we explicitly derive the advective transport term for the model, providing closure to the argument that active chiral matter can exhibit Euler turbulence.

We start with the discrete, slaved velocity,

$$\mathbf{v}_i = v_0(\cos \phi_i, \sin \phi_i).$$

We define a momentum density field  $\mathbf{g}(\mathbf{r}, t)$ , which in the discrete case becomes,

$$\mathbf{g}(\mathbf{r}, t) = \sum_{i=1}^N \mathbf{v}_i(t) \delta(\mathbf{r} - \mathbf{r}_i(t)), \quad (18)$$

where  $\delta(x)$  now defines the Dirac delta function. Next, take the time derivative  $\partial_t \mathbf{g}$ ,

$$\frac{\partial \mathbf{g}}{\partial t} = \underbrace{\sum_i \dot{\mathbf{v}}_i \delta(\mathbf{r} - \mathbf{r}_i)}_{\text{Orientation}} + \underbrace{\sum_i \mathbf{v}_i \frac{\partial}{\partial t} \delta(\mathbf{r} - \mathbf{r}_i)}_{\text{Transport} \equiv \mathcal{T}}, \quad (19)$$

where we identify the orientation term by noting that  $\dot{\mathbf{v}}_i$  contains the Kuramoto-like phase dynamics (Eq. 2). The second term is identified as momentum transport by the chain-rule property of the delta function, delta function  $\partial_t \delta(\mathbf{r} - \mathbf{r}_i) = -\nabla \cdot (\dot{\mathbf{r}}_i \delta)$ , as well as noting that  $\dot{\mathbf{r}}_i = \mathbf{v}_i$ ,

$$\mathcal{T} = -\nabla \cdot \left( \sum_i \mathbf{v}_i \mathbf{v}_i \delta(\mathbf{r} - \mathbf{r}_i) \right). \quad (20)$$

Simplifying the notation, we write,

$$\mathcal{T} = -\nabla \cdot \langle \mathbf{v}_i \mathbf{v}_i \rangle. \quad (21)$$

To see how Eq. (21) gives us an advective term  $(\mathbf{u} \cdot \nabla) \mathbf{u}$ , we must calculate the Tensor  $\langle \mathbf{v} \mathbf{v} \rangle$ . Consider the outer product  $\mathbf{v}_k \mathbf{v}_k$  and average it; specifically, the components (e.g.,  $xx$ ):

$$\langle v_x v_x \rangle = v_0^2 \langle \cos^2(\Psi + \delta\phi) \rangle, \quad (22)$$

using the expansion of  $\phi$  as a perturbation to the mean field. Using trigonometric identities and averaging over the fluctuations, we get,

$$\langle v_x v_x \rangle \approx \frac{v_0^2}{2} [1 + \underbrace{\langle \cos(2\delta\phi) \rangle}_{R_2} \cos(2\Psi)]. \quad (23)$$

where we identify the second-order order parameter  $R_2 \approx R^4$  (again assuming a peaked distribution), yielding an expression for *microscopic* stress. In the fluid phase (the Onsager dipole, Phase III), where the system exhibits marginal synchronization ( $0 < R < 1$ ), the fluctuations are dominated by frustration  $\omega_i$ , distinct from, and in

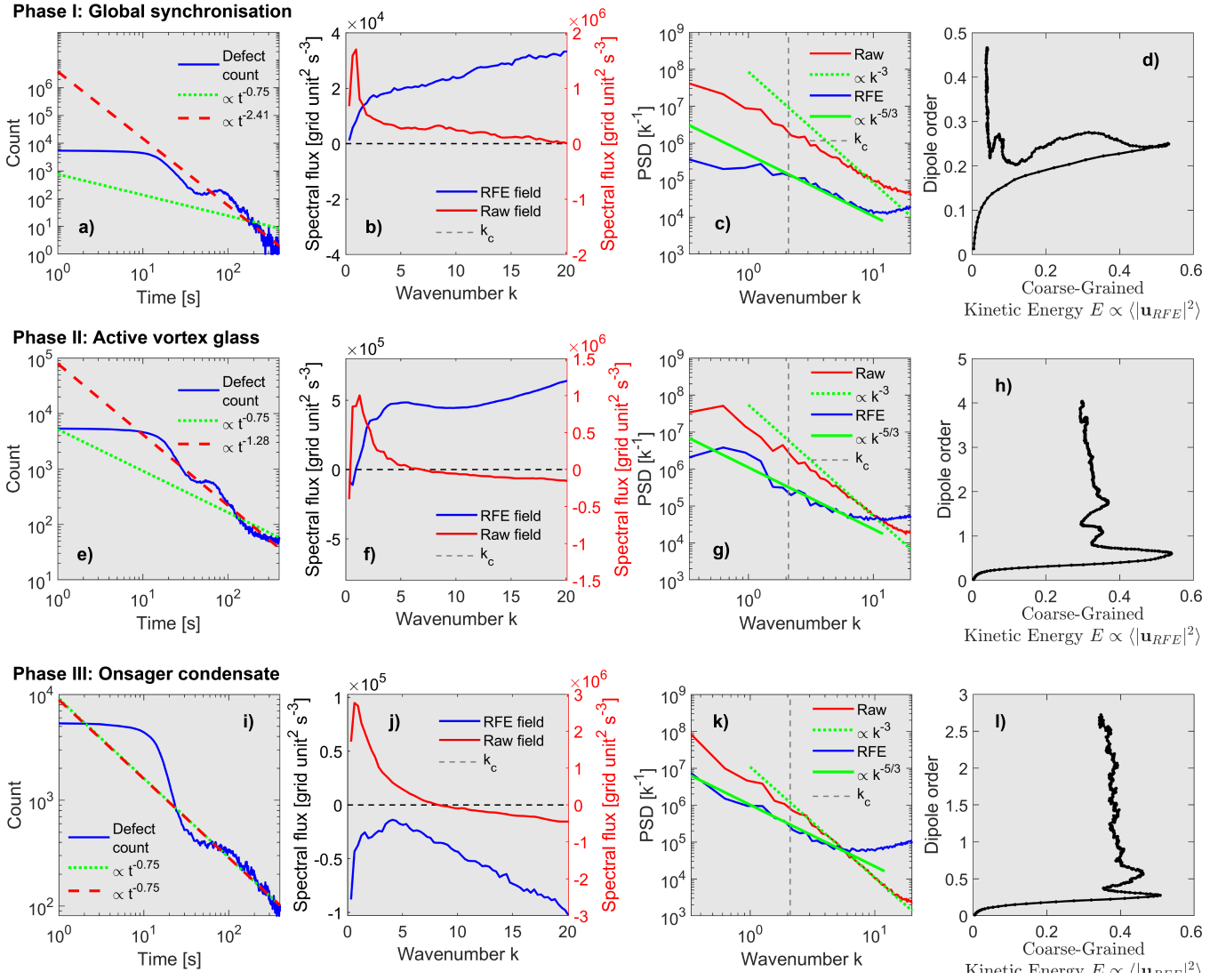


FIG. 6. Ensemble averages of 16 simulations, showing the behaviour of the three phases in Table I. The leftmost column (panels a, e, and i) show the defect count  $N_d(t)$  in a solid blue line, with a  $t^{-0.75}$  powerlaw in dotted green line and a fitted (through non-linear minimization of root-mean square error) powerlaw in dashed red line. The next column (panels b, f, and j) show median spectral flux for the raw (red) and RFE (blue) fields. The third column (panels c, g, and k) show the energy spectrum for the raw (red) and RFE (blue) fields, with  $k^{-3}$  and  $k^{-5/3}$  powerlaw fits, as well as the cut-off scale  $k_c$ . The last column (panels d, h, and l) show the thermodynamic trajectory. All quantities are shown as medians of 16 randomized (in initial locations  $x_i, y_i$  and white-noise  $\eta_i$ ) runs.

opposition to, the synchronization forces that maintain  $R$ .

For the equivalent expression for macroscopic stress, we use the definition of macroscopic velocity (Eq. 8),

$$u_x u_x = (v_0 R \cos \Psi)^2 = v_0^2 R^2 \cos^2 \Psi \quad (24)$$

Trigonometry again allows us to isolate the anisotropic part,

$$u_x u_x = \frac{v_0^2 R^2}{2} [1 + \cos(2\Psi)]. \quad (25)$$

Comparing Eqs. (23) and (24), we can now express the microscopic tensor as a function of the macroscopic

velocity plus an isotropic pressure term,

$$\langle v_x v_x \rangle = \underbrace{\frac{v_0^2}{2} (1 - R^2)}_{\equiv P_{\text{eff}}} + R^2 u_x u_x, \quad (26)$$

where  $P_{\text{eff}}$  is an effective pressure term generated by the incoherent, random fluctuations of the particles that are not aligned with the macroscopic flow, and where we identify the factor  $\lambda \equiv R^2$  as the *effective inertial mass*.

Substituting this closure back into the momentum con-

servation equation, we obtain:

$$\frac{\partial \mathbf{u}}{\partial t} + \lambda \nabla \cdot (\mathbf{u} \mathbf{u}) = -\nabla P_{\text{eff}} + \mathbf{F}_{\text{active}}, \quad (27)$$

where we identify  $F_{\text{active}} \approx \langle \sum \dot{v}_i \delta \rangle$  from Eq. (19) as a force vector that arise from the intrinsic frustration ( $\dot{v}_i$  depends on angular velocity  $\dot{\phi}_i \approx \omega_i$ ). While the system formally obeys the compressible Shallow Water equations (as derived in Eq. 12), in the limit where, we reiterate, the rotational, non-compressive modes dominate the irrotational, compressive modes, that is, the Onsager dipole, or Phase III in Table I, we recover the effective Euler advection term  $\lambda(\mathbf{u} \cdot \nabla) \mathbf{u}$ .

Finally, we clarify the role of the dispersion  $\Delta\omega$ . The magnitude of the active Reynolds stress scales with the velocity variance  $\langle \delta v^2 \rangle$ . Since the velocity fluctuations in the fluid limit are driven by the deviation of  $\phi_i$  from  $\Phi$ ,

Finally, we clarify the role of the dispersion  $\Delta\omega$ . The magnitude of the active Reynolds stress  $\tau_{\text{active}}$  scales with the velocity variance  $\langle \delta v^2 \rangle$ . To see why, observe that fluctuation in velocity  $\delta v_i$  is driven by the deviation of the particle's natural frequency  $\omega_i$  from the local mean frequency  $\Phi$ :

$$\delta v_i \sim \delta \dot{\phi}_i \approx (\omega_i - \Phi), \quad (28)$$

meaning that,

$$\langle \delta v \delta v \rangle \propto \langle (\omega_i - \Phi)^2 \rangle. \quad (29)$$

By definition, the variance of the natural phases  $\omega_i$  is the dispersion parameter squared:

$$\tau_{\text{active}} \propto \langle (\omega_i - \Phi)^2 \rangle \approx (\Delta\omega)^2. \quad (30)$$

Thus,  $\Delta\omega$  functions as the \*\*agitation parameter\*\* or granular temperature of the topological gas. This creates the central thermodynamic trade-off of the system: (1) Low  $\Delta\omega$  (Phase I): High synchronization ( $R \rightarrow 1$ ) but zero stress ( $\tau_{\text{active}} \rightarrow 0$ ). The fluid freezes into static clumps.

(2) High  $\Delta\omega$  (Phase III): High stress ( $\tau_{\text{active}}$  large) and marginal synchronization ( $0 < R < 1$ ). The system generates sufficient active stress to drive the inverse cascade, creating the “phantom inertia” that sustains the Onsager dipole.

Conversely, in Phase II, the active vortex glass, agitation  $\Delta\omega$  is insufficient to allow the system to overcome the lattice defect and access the negative-temperature regime of the Onsager dipole. Thus, ‘heating’ the microscopic degrees of freedom paradoxically leads to macroscopic ordering, a signature of non-equilibrium phase transitions where noise-induced coherence allows the emergence of large-scale transport [17].

## ACKNOWLEDGEMENTS

This work is supported by the European Space Agency's Living Planet Grant No. 1000012348. The au-

thor is grateful to O. Nestande, D. Knudsen, PT. Jayachandran, and K. Douch for stimulating discussions. Google's Gemini 3.0 Pro has been used for coding assistance in MATLAB.

---

\* Also at The European Space Agency Centre for Earth Observation, Frascati, Italy; Contact: magnus.fagernes@gmail.com

- [1] H. H. Wensink, J. Dunkel, S. Heidenreich, K. Drescher, R. E. Goldstein, H. Löwen, and J. M. Yeomans, Mesoscale turbulence in living fluids, *Proceedings of the National Academy of Sciences* **109**, 14308 (2012).
- [2] I. S. Aranson, Bacterial active matter, *Reports on Progress in Physics* **85**, 076601 (2022).
- [3] R. Alert, J. Casademunt, and J.-F. Joanny, Active Turbulence, *Annual Review of Condensed Matter Physics* **13**, 143 (2022).
- [4] M. Bourgoin, R. Kervil, C. Cottin-Bizonne, F. Raynal, R. Volk, and C. Ybert, Kolmogorovian Active Turbulence of a Sparse Assembly of Interacting Marangoni Surfers, *Physical Review X* **10**, 021065 (2020).
- [5] K. Qi, E. Westphal, G. Gompper, and R. G. Winkler, Emergence of active turbulence in microswimmer suspensions due to active hydrodynamic stress and volume exclusion, *Communications Physics* **5**, 49 (2022).
- [6] D. Saintillan and M. J. Shelley, Active suspensions and their nonlinear models, *Comptes Rendus Physique Living Fluids / Fluides Vivants*, **14**, 497 (2013).
- [7] J. K. Bhattacharjee and T. R. Kirkpatrick, Activity induced turbulence in driven active matter, *Physical Review Fluids* **7**, 034602 (2022).
- [8] J. Urzay, A. Doostmohammadi, and J. M. Yeomans, Multi-scale statistics of turbulence motorized by active matter, *Journal of Fluid Mechanics* **822**, 762 (2017).
- [9] V. Bratanov, F. Jenko, and E. Frey, New class of turbulence in active fluids, *Proceedings of the National Academy of Sciences* **112**, 15048 (2015).
- [10] L. Giomi, Geometry and Topology of Turbulence in Active Nematics, *Physical Review X* **5**, 031003 (2015).
- [11] J. Mecke, J. O. Nketsiah, R. Li, and Y. Gao, Emergent phenomena in chiral active matter, *National Science Open* **3**, 20230086 (2024).
- [12] M. T. Reeves, T. P. Billam, B. P. Anderson, and A. S. Bradley, Inverse Energy Cascade in Forced Two-Dimensional Quantum Turbulence, *Physical Review Letters* **110**, 104501 (2013).
- [13] M. Marmol, E. Gachon, and D. Faivre, Colloquium: Magnetotactic bacteria: From flagellar motor to collective effects, *Reviews of Modern Physics* **96**, 021001 (2024).
- [14] A. Maitra, Activity Unmasks Chirality in Liquid-Crystalline Matter, *Annual Review of Condensed Matter Physics* **16**, 275 (2025).
- [15] T. Markovich and T. C. Lubensky, Chiral active fluids: Insights from the total momentum, *Physical Review E* **112**, 035409 (2025).
- [16] M. F. Ivarsen, Spectral density characteristics of self-organized structuring in phase-synchronized oscillator ensembles (2025), arXiv:2508.21012 [physics].

[17] M. Y. Marov and A. V. Kolesnichenko, Self-Organization of Developed Turbulence and Formation Mechanisms of Coherent Structures, in *Turbulence and Self-Organization: Modeling Astrophysical Objects*, edited by M. Y. Marov and A. V. Kolesnichenko (Springer, New York, NY, 2013) pp. 373–423.

[18] L. Onsager, Statistical hydrodynamics, *Il Nuovo Cimento (1943-1954)* **6**, 279 (1949).

[19] J. A. Acebrón, L. L. Bonilla, C. J. Pérez Vicente, F. Ritort, and R. Spigler, The Kuramoto model: A simple paradigm for synchronization phenomena, *Reviews of Modern Physics* **77**, 137 (2005).

[20] F. De Smet and D. Aeyels, Partial entrainment in the finite Kuramoto–Sakaguchi model, *Physica D: Nonlinear Phenomena* **234**, 81 (2007).

[21] D. Helbing, Agent-Based Modeling, in *Social Self-Organization: Agent-Based Simulations and Experiments to Study Emergent Social Behavior*, edited by D. Helbing (Springer, Berlin, Heidelberg, 2012) pp. 25–70.

[22] V. Vijayan, K. K., S. J. J., and P. R., From disorder to design: Entropy-driven self-organization in an agent based swarming model and pattern formation, *Chaos, Solitons & Fractals* **200**, 116894 (2025).

[23] K. K. Dey, Dynamic Coupling at Low Reynolds Number, *Angewandte Chemie International Edition* **58**, 2208 (2019).

[24] W. Y. Tan, *Shallow Water Hydrodynamics: Mathematical Theory and Numerical Solution for a Two-dimensional System of Shallow-water Equations* (Elsevier, 1992).

[25] C. B. Vreugdenhil, *Numerical Methods for Shallow-Water Flow* (Springer Science & Business Media, 2013).

[26] R. Delabays, T. Coletta, and P. Jacquod, Multistability of phase-locking and topological winding numbers in locally coupled Kuramoto models on single-loop networks, *Journal of Mathematical Physics* **57** (2016).

[27] Y. N. Ovchinnikov and I. M. Sigal, The energy of Ginzburg–Landau vortices, *European Journal of Applied Mathematics* **13**, 153 (2002).

[28] D. E. Pelinovsky and P. G. Kevrekidis, Variational approximations of trapped vortices in the large-density limit, *Nonlinearity* **24**, 1271 (2011).

[29] R. H. Kraichnan, Inertial-range transfer in two- and three-dimensional turbulence, *Journal of Fluid Mechanics* **47**, 525 (1971).

[30] V. Borue, Spectral exponents of enstrophy cascade in stationary two-dimensional homogeneous turbulence, *Physical Review Letters* **71**, 3967 (1993).

[31] V. Borue, Inverse energy cascade in stationary two-dimensional homogeneous turbulence, *Physical Review Letters* **72**, 1475 (1994).

[32] M. Chertkov, C. Connaughton, I. Kolokolov, and V. Lebedev, Dynamics of Energy Condensation in Two-Dimensional Turbulence, *Physical Review Letters* **99**, 084501 (2007).

[33] A. N. Kolmogorov, LOCAL STRUCTURE OF TURBULENCE IN AN INCOMPRESSIBLE VISCOUS FLUID AT VERY HIGH REYNOLDS NUMBERS, *Soviet Physics Uspekhi* **10**, 734 (1968).

[34] S. B. Pope, *Turbulent Flows* (Cambridge: Cambridge University Press, 2000).

[35] G. F. Carnevale, J. C. McWilliams, Y. Pomeau, J. B. Weiss, and W. R. Young, Evolution of vortex statistics in two-dimensional turbulence, *Physical Review Letters* **66**, 2735 (1991).

[36] J. D. Buntine and D. I. Pullin, Merger and cancellation of strained vortices, *Journal of Fluid Mechanics* **205**, 263 (1989).

[37] F. Rizzi and L. Cortelezzi, Stirring, stretching and transport generated by a pair of like-signed vortices, *Journal of Fluid Mechanics* **674**, 244 (2011).

[38] S. Shankar, A. Souslov, M. J. Bowick, M. C. Marchetti, and V. Vitelli, Topological active matter, *Nature Reviews Physics* **4**, 380 (2022).

[39] S. Mondal, P. Popli, and S. Sarkar, Coarsening dynamics of aster defects in model polar active matter, *Soft Matter* **21**, 77 (2025).

[40] J. G. Esler, Equilibrium energy spectrum of point vortex motion with remarks on ensemble choice and ergodicity, *Physical Review Fluids* **2**, 014703 (2017).

[41] T. Tanogami and S.-i. Sasa, A Simple XY Model for Cascade Transfer (2022), arXiv:2106.11670 [cond-mat].

[42] A. S. Bradley and B. P. Anderson, Energy Spectra of Vortex Distributions in Two-Dimensional Quantum Turbulence, *Physical Review X* **2**, 041001 (2012).

[43] M. James, W. J. T. Bos, and M. Wilczek, Turbulence and turbulent pattern formation in a minimal model for active fluids, *Physical Review Fluids* **3**, 061101 (2018).

[44] M. Linkmann, G. Boffetta, M. C. Marchetti, and B. Eckhardt, Phase Transition to Large Scale Coherent Structures in Two-Dimensional Active Matter Turbulence, *Physical Review Letters* **122**, 214503 (2019).

[45] S. Mukherjee, R. K. Singh, M. James, and S. S. Ray, Intermittency, fluctuations and maximal chaos in an emergent universal state of active turbulence, *Nature Physics* **19**, 891 (2023).

[46] K. V. Kiran, K. Kumar, A. Gupta, R. Pandit, and S. S. Ray, Onset of Intermittency and Multiscaling in Active Turbulence, *Physical Review Letters* **134**, 088302 (2025).